Microtubules are not passive load-bearing elements in axon growth

Vittoria Raffa

vittoria.raffa@unipi.it

University of Pisa https://orcid.org/0000-0002-4289-9937

Lorenzo Da Palmata

University of Pisa

Tiziana Schmidt

University of Pisa https://orcid.org/0000-0002-6477-115X

Allegra Coppini

University of Pisa

Francesco Simoni

University of Pisa

Elena Landi

University of Pisa

Matteo Coppoletta

University of Pisa

Peter Bluemler

University of Mainz https://orcid.org/0000-0002-0412-7549

Jesús García

Universidad de Zaragoza

Gerardo Goya

1Instituto de Nanociencia y Materiales de Aragón (INMA), CSIC-Universidad de Zaragoza
https://orcid.org/0000-0003-1558-9279

Laura Marchetti

University of Pisa

Biological Sciences - Article

Keywords: mictrobule, force, axon, mechanotransduction

Posted Date: April 7th, 2026

DOI: https://doi.org/10.21203/rs.3.rs-8911112/v1

Additional Declarations: There is **NO** Competing Interest.

Abstract

Axons are sensitive to piconewton (pN) forces, yet the cellular mechanisms underlying this mechanosensitivity remain poorly understood. Axonal mechanotransduction has traditionally been attributed to molecular clutches and mechanosensitive ion channels, whereas cytoskeletal microtubules (MTs) have been regarded primarily as passive load-bearing structures. Here, we propose MTs as active elements in signal mechanotransduction. Using nano-pulling to apply controlled, directional pN forces to hippocampal neurons, we show that force induces axon elongation only when applied along the intrinsic polarity of axonal MTs. Live imaging of the MT plus-end marker EB3 reveals modulation of MT dynamics and enhanced MT growth when force is applied along MT polarity, but not in the opposite direction. Strikingly, restricting force generation to the axolemma, thereby uncoupling mechanical inputs from the axonal cytoskeleton, abolishes force-induced axon elongation.

Main

Forces in the piconewton (pN) range exert a profound influence on axonal development, modulating multiple processes such as extension, branching, pruning, synapse formation, and axon fasciculation.[1] This raises the fascinating question of how axons sense and transduce piconewton-level forces and what the principles of mechanotransduction are. Historically, the mechanosensitive (MS) components of the axon have been considered to be the molecular clutches at point contact (PC) adhesions and mechanosensitive ion channels (MSCs). Piconewton forces promote adhesion maturation by inducing conformational changes in many mechanosensitive proteins of the molecular clutches and exposing cryptic domains.[2–5] Forces in the 10-30 pN range prolong the bond lifetimes between integrins and their ligands.[6] MSCs such as Piezo1 stabilize in the open state in response to a 10 pN force.[7] For example, in hippocampal neurons a mechanical force of 13 pN is sufficient for inducing an intracellular Ca^{++} influx through transmembrane ion channels, resulting in axon retraction.[8]

In this paper, we focus our attention on microtubules (MTs). Traditionally, MTs have not been considered mechanosensitive, as they are rigid load-bearing elements. MTs have a Young's modulus of approximately 1.2 gigapascals (GPa), and pN forces are not sufficient to cause stretching or strain in individual MTs. However, recent studies suggest that mechanical stress can be stored within the MT lattice, inducing changes in MT polymerization dynamics.[9]

MTs have a polar structure composed of αβ-tubulin heterodimers arranged in (most commonly) 13 protofilaments.[10] Interactions between adjacent dimers occur through lateral and longitudinal non-covalent bonds. The plus end typically grows faster than the minus end.[11] When a dimer is incorporated into a growing microtubule, GTP is hydrolyzed. The transition from GTP-tubulin to GDP-tubulin at the growing tip likely destabilizes lateral bonds, as a portion of the free energy liberated by this chemical reaction is stored as curvature strain in the microtubule lattice,[12] leading to plus-end instability.[13] Interestingly, theoretical studies show that a pN-scale pulling force facilitates lateral bond formation

between adjacent dimers, thereby promoting protofilament wall closure and enhancing MT assembly at the plus end.[14] This model is supported by experimental data demonstrating that a traction force of 0.5-2 pN decreases the probability of catastrophe in growing MTs and increases the probability that short MTs resume growth.[15]

In previous studies, we employed nano-pulling to mechanically stretch axons of hippocampal neurons. In this approach, magnetic nanoparticles (MNPs) are administered to stage 1 neurons, where they localize within the axoplasm and interact with axonal cytoskeletal components.[16] The application of a controlled magnetic field gradient generates a force vector that stretches the magnetized axon. Using this strategy, we demonstrated that nano-pulling promotes axon elongation; however, this effect is abolished by nocodazole treatment, but not by paclitaxel, blebbistatin, or cytochalasin B.[16] These findings suggest a central role for MT dynamics - specifically MT stabilization - in force-induced axon growth. Consistent with this hypothesis, we observed a marked accumulation of MTs within stretched axons.[16,17]

Genetic manipulation of α- or β-tubulin is not compatible with survival in mammals; however, in *C. elegans*, loss of α- or β-tubulin orthologs is tolerated, as MTs can still assemble into less stable structures composed of 11 protofilaments rather than the canonical 13. Exploiting this model, we demonstrated that nano-pulling fails to induce axon growth in *C. elegans* neurons lacking either α- or β-tubulin orthologs.[17] Together, these observations strongly support MTs as key mediators of mechanotransduction during axon elongation.

In the present study, we explore the relationship between nano-pulling and microtubules, with particular emphasis on MT polarity. Axonal MTs are known to display a preferential polarity, with plus-ends oriented toward the distal tip, whereas dendritic MTs exhibit mixed polarity.[18] Given that nano-pulling enables the application of a force vector with defined amplitude, direction, and orientation,[19] we tested the hypothesis that force-induced axon growth follows the intrinsic polarity of axonal MTs. Finally, we show that when MNPs are restricted to the plasma membrane - thus preventing direct force transmission to MTs - nano-pulling is no longer able to promote axon growth, further highlighting the essential role of MTs in this mechanotransduction process.

Results

Nano-pulling modifies neuron morphology

Here, in order to apply a unidirectional force, we used a bridge-shaped magnetic applicator that was characterized in a previous work.[20] The device generates an on-axis force along the microchannel in which neurons grow ($d|B|/dx \approx 20$ T m^{-1}, whereas $d|B|/dy$, $d|B|/dz \approx 0$) within a region of a few millimeters where images were acquired (Figure S1).

To characterize the effects of force-induced axon growth (hereafter referred to as stretch-growth) neuronal morphology (somata, dendrites, and axons) was automatically reconstructed using

Neurolucida-based tracing (Figure 1A1-2). Consistent with previous observations,[16] nano-pulling induced axonal growth (Figure 1C1-3). Stimulated neurons exhibited significantly longer axons than controls (134.9 ± 4.0 μm and 173.2 ± 4.7 μm for the control and stretch groups, respectively; $p < 0.0001$), accompanied by marked increases in axonal surface area (+47.3%, $p < 0.0001$) and volume (+101.7%, $p < 0.0001$), indicative of extensive axonal remodeling.

Dendritic morphology was assessed by comparing mean dendritic length, surface area, and volume between conditions (Figure 1C4-C6). While dendritic length was not affected by stimulation ($p = 0.94$), stimulated neurons showed a significant increase in dendritic surface area (+22.1%, $p < 0.0001$) and volume (+40.3%, $p < 0.0001$). These results indicate that nano-pulling selectively increases dendritic caliber rather than dendritic elongation.

Analysis of soma morphology revealed that nano-pulling does not affect overall soma geometry, as no changes were detected in soma area ($p = 0.46$, Figure 1C7) or roundness ($p = 0.95$, Figure 1C8).

Stretch-growth depends on force orientation

Since microtubules in stage 3 neurons are preferentially oriented with their (+) end toward the growth cone[18] (Figure 2A1), we investigated whether nano-pulling depends on force orientation. The bridge-shaped magnetic applicator used here generates a constant force along the microchannel within the region of interest (ROI, Figure S1), and the angular component of neurites in the xz plane can be automatically measured using Neurolucida software.

To determine whether axonal growth was influenced by force orientation, axon length was analyzed using polar histograms and xz angle classification (Figure 2B1). The two data distributions were found to be statistically different ($p < 0.0001$). In the control group, the angular distribution of axon length appears to be random, whereas stretched axons exhibit greater lengths at smaller angles (Figure 2B1). Axons were then grouped according to their growth direction, either along or opposite to the magnetic force (Figure 2A2). Specifically, an angular threshold of 30° was set: axons were classified as force (+) when $330° < \theta < 30°$, corresponding to a positive on-axis force component ( ), and as force (-) when $150° < \theta < 210°$, corresponding to a negative on-axis force component ( ).

The distribution of axons between the force (+) and force (-) groups differed significantly between control and stretched conditions, with a higher fraction of stretched axons growing in the force (+) orientation ($p = 0.013$, Figure 2B2). Interestingly, nano-pulling induced stretch-growth in the force (+) group ($p < 0.0001$), but not in the force (-) group ($p = 0.2$) (Figure 2B3). Specifically, in the force (+) group, axon length increased from 112.7 ± 5.1 μm in control axons to 201.5 ± 7.8 μm in stretched axons, corresponding to a 79% increase.

Since MTs are randomly oriented in dendrites, we hypothesized that nano-pulling would not be influenced by force orientation. To test this hypothesis, dendrites were classified according to their orientation with respect to the applied force, similarly to axons. Dendrite length showed a similar random

angular distribution between the control and stretched conditions (p = 0.88, Figure 2C1). Moreover, when dendrites were categorized based on their alignment with the magnetic force, the fraction of dendrites growing in the force (+) or force (-) orientation did not differ between control and stretched conditions (p = 0.68, Figure 2C2). No significant differences were detected in either length (Figure 2C3) or surface area (Figure 2C4) between stretched and control dendrites, regardless of whether they were growing in the force (+) orientation (length: p = 0.68; surface area: p = 0.90) or in the force (-) orientation (length: p = 0.71; surface area: p = 0.55).

Stretch-growth depends on force localization

Neuronal mechanotransduction has classically been attributed to force generation at mechanosensitive channels localized at the plasma membrane.[21,22] Here we propose a conceptual shift, suggesting that mechanotransduction signaling is mediated by microtubules rather than MSCs. To test this hypothesis, we engineered MNPs to relocate the site of force application from the axoplasm, that contains dense bundles of microtubules, to the axolemma, where MSCs are located.

MNPs were designed to self-assemble onto a recombinant protein comprising an iron-binding domain, a fluorescent reporter for cell tracking, and a membrane-targeting domain (Figure 3A). As the iron-binding module driving MNP assembly, we selected the C-terminal region of Mms6, a magnetosome-specific protein from magnetotactic bacteria that exhibits strong affinity for the magnetite inorganic core.[23] This intrinsic property of Mms6 has been previously exploited for the direct conjugation of MNPs. [24]. A fluorescent reporter (GFP) was fused to ΔN-Mms6 (hereafter Mms6) to enable visualization and tracking. To direct force generation specifically to the plasma membrane, we employed the Lck membrane-targeting domain, chosen for its robust characterization, widespread use, and high specificity for membrane localization.[25] The Lck-GFP-Mms6 construct and the same construct without the localization domain (GFP-Mms6) were generated. The presence of both proteins of interests (POIs) was monitored by western blotting (Figure 3B). The purified recombinant proteins GFP-Mms6 and Lck-GFP-Mms6 did not elicit detectable neurotoxic effects, even when administered at millimolar concentrations (Figure 3C).

MNPs with a bare iron oxide surface were synthesized to enable efficient Mms6 binding. Commercially available MNPs were unsuitable for this application due to the presence of an organic corona required for particle stabilization and dispersion, which interferes with iron oxide Mms6 recognition. Home-made MNPs were synthesized following the protocol described by Shipunova and colleagues, who extensively characterized the use of ΔN-Mms6 as a natural iron-binding linker.[24,26]

Transmission electron microscopy (TEM) analysis (Figure 3D) revealed nanoparticles with a spherical-parallelepiped morphology and an average diameter of 12 ± 2 nm (Figure 3E). Magnetic characterization performed with a Superconducting Quantum Interference Device Magnetometer (SQUID) at T=6K and 325K were consistent with the Fe_3O_4 (magnetite) ferrimagnetic behavior at low temperature (Figure 3F). At room temperature, the particles exhibited superparamagnetic properties, characterized by negligible

coercivity and remanence. The measured saturation mass magnetization at H=5T and room temperature was M_S= 76.22 emu·g^{-1}, while 90% of the M_S value was already reached at H=0.5 T.

Primary hippocampal neurons were incubated with home-made MNPs for 72 h. No cell detachment - an early indicator of nanoparticle-induced toxicity - was observed within the tested concentration range (1.8-7.4 µg mL^{-1}; Figure 3G). The absence of cytotoxic effects was further supported by axonal length measurements, which remained unchanged following MNP treatment (Figure S2).

Since nanoparticle integrity is a critical requirement for nano-pulling experiments, MNP degradation was assessed by quantifying intracellular iron content over time. Detectable degradation began after 72 h of incubation, indicating that the nanoparticles remained structurally intact up to this time point. A significant increase in intracellular iron was detected 18 days post-incubation, suggesting slow degradation kinetics (Figure 3H). This result is particularly relevant for the proposed approach, as it ensures MNP integrity throughout the mechanical stretching protocol.

Home-made MNPs were subsequently evaluated for their ability to induce stretch-growth and they consistently promoted axon outgrowth in a dose-dependent manner (Figure S3). As comparable effects were observed at concentrations ≥ 3.7 µg mL^{-1}, this concentration was selected as the standard working concentration for subsequent experiments.

Recombinant proteins were then conjugated to bare MNPs by exploiting the iron-binding properties of the Mms6 domain. The optimal protein-of-interest (POI) to MNP molar ratio was determined to be in the range of 1:10-20 (POI:MNP). Successful protein conjugation was confirmed by Fourier-transform infrared (FTIR) spectroscopy (Figure 3I, see supplementary data).

Dynamic light scattering analysis revealed a modest increase in hydrodynamic diameter and polydispersity index (PI) following protein conjugation, indicating successful functionalization without inducing particle aggregation (bare MNPs: d = 54.98 nm, PI = 0.220; Lck-GFP-Mms6:MNPs: d = 68.3 nm, PI = 0.285; GFP-Mms6:MNPs: d = 68.55 nm, PI = 0.227; Figure 3L). All MNP formulations exhibited a zeta potential > 30 mV, consistent with stable colloidal dispersions. As both POIs carry a net negative charge at their isoelectric point, protein conjugation shifted the surface charge of the MNPs toward less cationic values (bare MNPs: 41.9 ± 12.6 mV; Lck-GFP-Mms6:MNPs: 34.2 ± 14 mV; GFP-Mms6:MNPs: 32.1 ± 13.3 mV, n = 3). Protein conjugation efficiency was further confirmed by dot blot analysis (Figure 3M). When neurons were incubated with either Lck-GFP-Mms6:MNPs or GFP-Mms6:MNPs, no toxicity was observed within the tested concentration range (1.8-5.5 µg mL^{-1}; Figure 3N).

Prior to performing the stretching experiments, we first assessed the subcellular localization of the recombinant proteins. As a model system, we used neuron-like PC12 cells differentiated with nerve growth factor (NGF), as their enlarged soma enables high-resolution analysis of protein distribution by confocal microscopy. As expected, GFP-Mms6 displayed a diffuse cytoplasmic distribution, whereas Lck-GFP-Mms6 was predominantly localized at the plasma membrane in NGF-stimulated PC12 cells (Figure 4A).

After confirming efficient plasma membrane targeting of the Lck-tagged construct, PC12 cells were subjected to nano-pulling (Fig. 4B). Neurite length was significantly increased in cells incubated with GFP–Mms6:MNPs (Fig. 4C1, $p = 0.0046$), whereas no significant enhancement was observed in cells treated with Lck–GFP–Mms6:MNPs (Fig. 4C2, $p = 0.65$). Thus, the stretch-growth response was dependent on the fusion protein used to functionalize the MNPs.

Consistently, in hippocampal neurons, GFP–Mms6:MNP treatment induced robust stretch-growth (Fig. 4D1, $p < 0.0001$), while neurons treated with Lck–GFP–Mms6:MNPs showed no significant difference in axon length between control and stretched conditions (Fig. 4D2, $p = 0.84$).

Because the only distinction between the two types of functionalized MNPs lies in the presence of the targeting domain, these results indicate that membrane confinement of force generation interferes with the cellular stretch-growth response. This outcome is consistent with our initial hypothesis, as the experimental design was intended to apply mechanical forces to distinct subcellular compartments, thereby eliciting differential cellular responses.

Nano-pulling alters microtubule post-translational modification

Microtubules undergo a variety of post-translational modifications (PTMs), collectively referred to as the “tubulin code” or “tubulome”, which regulate MT stability, dynamics, and interactions with microtubule-associated proteins (MAPs).[27] In this study, we focused on PTMs that are commonly associated with alterations in MT stability in presence of mechanical stimuli (Figure 5A1). In particular, long-lived stable axonal MTs are generally characterized by an enrichment in acetylated[28] and glutamylated[29] and detyrosinated [30] tubulin.

Consistent with our previous findings, mechanical stretching induced a significant increase in the acetylated-to-tyrosinated α-tubulin ratio (acTUBA/tyrTUBA), a widely used indicator of MT stability,[17,31,32] both in neuronal somata (Figure 5B2, $p < 0.0001$) and axons (Figure 5B3, $p < 0.0001$). However, treatment of neurons with nocodazole (Ncz) at a concentration previously shown not to interfere with spontaneous axon growth but sufficient to inhibit stretch-growth,[16] prevented the nano-pulling-induced increase in the acTUBA/tyrTUBA ratio in both somata (Figure 5B2, $p = 0.13$) and axons (Figure 5B3, $p = 0.06$).

We next assessed the levels of tubulin polyglutamylation. Polyglutamylation consists of the addition of glutamate residues to internal glutamate sites within the C-terminal tails of tubulin, generating branched polyglutamate side chains that typically reach a length of 4-6 residues.[33] Given that enrichment of polyglutamylated MTs has been reported in mature neurons,[34] analyses were performed at DIV9. Neurons were immunostained with an antibody recognizing most forms of polyglutamylated tubulin (poly-glut), independent of side-chain length and tubulin isoform (α- or β-tubulin), and with an antibody specific for glutamate chains composed of four or more residues (poly-E).

Stretching resulted in a significant increase in both poly-glut (Figure 5C2, $p = 0.003$) and poly-E (Figure 5C3, $p = 0.041$) normalized signal intensities. Notably, we also observed a significant increase in the

poly-glut/poly-E ratio (Figure 5C4, $p = 0.0001$), suggesting a more pronounced effect of mechanical stretching on the initiation of polyglutamate side chains rather than on their elongation.

Nano-pulling alters MT dynamics

To investigate growing neuronal MTs, neurons were infected with lentiviral vectors expressing an RFP-tagged construct of EB3 (Figure 6A), a plus-end-binding protein. EB3 comets were tracked along the axon (Figure 6B1) and within growth cones (Figure 6B2) (Supplementary Video). EB3 comet dynamics were analyzed over 60 frames, and kymographs were generated (Figure 6B3).

Based on our previous work demonstrating that nano-pulling increases axonal MT density by approximately 40%,[17] we quantified the density of fluorescently labeled EB3 comets as a proxy for growing MTs. Consistent with this hypothesis, we observed a significant increase in comet density in stretched axons (Figure 6C1, $p < 0.0001$). Notably, this increase was restricted to axons growing in the direction of the applied force (force (+)), showing a 90% increase (0.48 ± 0.045 comets per μm² in control axons vs. 0.91 ± 0.093 comets per μm² in stretched axons, $p < 0.0001$). In contrast, no increase was detected in stretched axons growing opposite to the force direction (force (-)) (0.48 ± 0.045 comets per μm² in control axons vs. 0.50 ± 0.046 comets per μm² in stretched axons, $p = 0.98$).

Analysis of comet specific dynamic populations revealed that this increase was primarily attributable to anterograde comets (0.31 ± 0.038 comets per μm² in control axons, 0.56 ± 0.067 comets per μm² in force (+) axons, and 0.32 ± 0.038 comets per μm² in force (-) axons). The increase in anterograde comets between control axons and axons growing in the force direction was 81% (Figure 6C2, $p = 0.003$). No significant differences were observed for retrograde comets (Figure 6C3, $p = 0.07$).

Similarly, at the level of the GC, an increase in the density of RFP-EB3 comets was detected only at tips growing in the same orientation as the applied mechanical stimulus (force (+)). Under these conditions, comet density increased from 0.54 ± 0.068 comets per μm² in control GCs to 0.89 ± 0.086 comets per μm² in stretched GCs, corresponding to a 65% increase (Figure 6C4, $p = 0.0012$). In contrast, GCs growing in the opposite direction of the applied force (force (-)) did not show any significant change in comet density compared to controls (0.52 ± 0.061 comets per μm², $p > 0.99$). When EB3 comets were classified according to their dynamic behavior, this effect was again found to be specifically associated with anterograde-moving comets. In particular, the density of anterograde comets increased to 0.48 ± 0.046 comets per μm² in GCs oriented along the force (+), compared with 0.22 ± 0.029 comets per μm² in control GCs, while remaining unchanged in force (-) GCs (0.27 ± 0.032 comets per μm²). This selective enrichment corresponds to an 118% increase in anterograde comets in GCs growing along the applied force (Figure 6C5, $p < 0.0001$). No statistically significant differences were observed for retrograde comets (Figure 6C6, $p = 0.073$).

Moreover, we analyzed the velocity of RFP-EB3 comets with respect to the axonal compartment (central axon and GC) and the direction of movement (anterograde or retrograde). In central axons, anterograde comets correspond to growing MTs oriented with their (+) end toward the growing tip. Their velocity was

significantly higher than in control axons (0.036 ± 0.0030 μm s^{-1}) when axons were stretched in the force (+) orientation (0.071 ± 0.0059 μm s^{-1}), representing a 97% increase ($p < 0.0001$, Figure 6D1). In contrast, anterograde comets in axons growing in the force (−) orientation did not show a significant difference compared with control axons (0.041 ± 0.0032 μm s^{-1}, $p = 0.83$, Figure 6D1). Notably, no statistically significant differences were detected among control, force (−), and force (+) groups in the velocity of retrograde comets (Figure 6D2).

Velocity analysis revealed a different behavior in GCs, where growing MTs are more dynamic and undergo continuous MT recycling. The velocities of both anterograde and retrograde comets varied markedly within GCs. When GCs were stretched in the force (+) orientation, anterograde comets exhibited a 98% increase in speed ($p < 0.0001$, Figure 6D3), while retrograde comets showed an 80% increase in speed ($p = 0.0024$, Figure 6D4). In contrast, neither anterograde (Figure 6D3, $p = 0.85$) nor retrograde (Figure 6D4, $p = 0.26$) comets in GCs growing in the force (−) orientation differed significantly from those in control GCs.

The analysis of the fraction of time that EB3 comets spent in the growing and paused states showed a decrease in pauses in anterograde comets when axons were stretched in the force (+) orientation ($p = 0.0016$), but not in the force (−) orientation ($p = 0.77$) (Figure E1). The same behavior was observed for anterograde comets in the CG (Figure E3). Conversely, for retrogradely moving comets, no statistically significant differences were detected among the groups (Figures E2 and E4).

Discussion

Axon growth has classically been interpreted in the context of cytoskeletal dynamics occurring at the growth cone. During chemotaxis, a chemoattractant cue (e.g., netrin-1, NGF, BDNF) binds to its receptor at the growth cone, activating intracellular signaling cascades that promote PC adhesion maturation and a concomitant reduction in actin retrograde flow.[35–38] This process generates contractile forces that both push the growth cone forward and pull the axon shaft ahead.[39] Specifically, the pushing component supports protrusive growth at the leading edge, whereas the pulling component induces bulk translocation of MT bundles, which are mechanically coupled to actin filaments within the growth cone.[40–42]

Within this classical framework, microtubules are generally considered passive elements that interact with the actin cytoskeleton but do not actively contribute to force sensing or mechanotransduction. In contrast, here we propose that the pulling forces acting along the axon shaft can directly sustain axon elongation by acting at the level of microtubules themselves. This possibility has remained largely unexplored, in part because conventional experimental approaches - such as restrained bead interaction assays[43] - primarily generate forces localized at the growth cone. In the present study, we employed nano-pulling, a technique with the distinct advantage of applying mechanical stretch intracellularly along the entire axon. We found that nano-pulling induces sustained axon growth (Figure 1C1-C3). Interestingly, nano-pulling promoted elongation in axons but not in dendrites (Figure 1C4). In light of a

possible involvement of MTs, this observation may be related to the fact that, in axons—but not in dendrites—the majority of MTs are uniformly polarized, with their plus ends oriented toward the growth cone. Nano-pulling proved to be an ideal approach to test this hypothesis, as it allows precise control over the orientation of the applied force. Consistent with this idea, we observed that nano-pulling induces axon growth only when the force vector is aligned with the intrinsic polarity of axonal MTs (Figure 2).

The mechanism underlying force-mediated axon outgrowth is still elusive, and the involvement of the axonal cytoskeleton remains controversial. Among the classes of mechanosensitive proteins involved in the capturing of incoming mechanical stimuli and their forwarding to diverse downstream mechanisms, MS channels have historically attracted the most attention.[44] In this paper, in order to elucidate which MS component is responsible for force-mediated axon growth, we designed and validated a tool for precise subcellular localization, enabling targeted application of mechanical stimulation at the cell membrane, where MSCs are mainly located.

Following the characterization of the synthetized MNPs (Figure 3), we investigated whether the presence or absence of a cell membrane localization signal could lead to a differential cellular response. The underlying hypothesis was that the axoplasmic localization of MNPs facilitates mechanotransduction at the axonal MT level, while localization of MNPs to the axolemma might stimulate MSCs.[8,21] Consistent with the previously obtained results (Figure 1C1), MNPs without the localization signal induced axon growth, whereas treatment with MNPs harboring the cell membrane localization signal resulted in no detectable response (Figure 4). These results were confirmed in two models (PC12 cells differentiated with NGF and hippocampal neurons). Overall, the obtained results strongly indicate that axon elongation is induced only when mechanical stimulation can be perceived at the level of the axoplasm.

We next focused on axonal MTs to identify force-induced alterations at this level. Theoretical studies predict that MT growth can be accelerated several-fold by the application of a plus-end-directed pN force.[14] To experimentally test this model in the axons of living neurons, we tracked the plus-end binding protein EB3, since the movement of GFP-EB3 comets reflects MT polymerization dynamics.[45] We found that the velocity of comets in the axon increased in response to force only when the force was applied in the axon growth orientation (i.e. when axonal MTs are exposed to a plus-end force). In fact, this effect was observed for anterograde comets (Figure 6D1) but not for retrograde comets (Figure 6D2). Interestingly, in the growth cone, a force applied in the growth orientation accelerated the speed of both anterograde and retrograde comets (Figure 6D3-4). We interpret this difference as a consequence of the highly dynamic MT organization in the growth cone, where growing MTs invading the peripheral domain are rapidly recycled back to the central domain (see Supplementary Video 2).

The model proposed by Gudimchuk and colleagues posits that a plus-end force accelerates MT assembly by promoting lateral bond formation between GTP–tubulin dimers, thereby stabilizing protofilament structure and preventing disassembly.[14] Consistent with this mechanism, we found that the increase in comet velocity is accompanied by a reduction in pause duration (Fig. 6E), indicating that

MTs spent more time in the growing state and less in the paused state, when force was applied in the direction of axon elongation. Further supporting this mechanism, the density of growing MTs increased only when the force is applied in this orientation (Fig. 6C1). Notably, this effect was specific to the anterograde comet population (Fig. 6C2) and was not observed in retrograde comets (Fig. 6C3). The same trend was evident both along the axon shaft (Fig. 6C1–3) and within the growth cone (Fig. 6C4–6).

Since stable MTs exhibit a distinctive tubulome, we investigated specific PTMs typically associated with long-lived MTs. We found that nano-pulling promotes the initiation of polyglutamylation chains within the C-terminal tails of tubulin (Figure 5C), a modification that has recently been proposed as part of a mechanically driven mechanism for MT stabilization.[29]

In stretched axons, we also observed an increased ratio of acetylated versus tyrosinated α-tubulin (Figure 5B). However, no detectable differences between control and stretched axons were observed when neurons were treated with nocodazole, a drug that blocks nano-pulling-induced axon growth.[16] This PTM profile is consistent with a stabilizing effect, as α-tubulin detyrosination generates disassembly-resistant protofilaments,[46] while α-tubulin acetylation increases MT flexibility, prolongs MT half-life, and enhances mechanical resilience, including under mechanical stimulation.[28,47,48]

In conclusion, our experimental data support a model in which plus-end–directed forces acting on MTs within living axons stabilize the MT lattice, reduce pause duration, and accelerate MT growth. This process results in an increased linear density of MTs along the axon shaft of hippocampal neurons.[16] We demonstrated in previous work that such accumulation has major functional implications,[1] as the axon shaft is predominantly composed of parallel MT bundles that provide the structural backbone required for efficient axonal transport. From a biophysical perspective, an increased MT content within the axon enhances the pulling forces generated by MT polymerization and sliding. These forces oppose the contractile tension produced by the axonal actin cortex and transmitted to the GC.[49] A relative reduction in contractile forces within the axon shaft is known to favor forward growth GC and axon elongation.[50] Beyond their structural and mechanical roles, the accumulation of axonal MTs also impacts gene expression regulation at the post-transcriptional level. In fact, increased MT density promotes the transport of organelles and vesicles within the axon shaft, thereby promoting activation of local translational.[17] This functional coupling between axonal transport and local protein synthesis provides the additional mass required to sustain nano-pulling-induced axon growth, linking responsiveness of MTs to mechanical stimuli to long-term structural remodeling of the axon.

Methods

Data availability

Authors declare to adhere to OS principles. Raw data, metadata, processed data associated to this publication are available in Zenodo repository (link available after acceptance).

Mice

All animal experiments were conducted in full accordance with the protocols approved by the Italian Ministry of Public Health and the Ethical Committee of the University of Pisa (protocol no. AC179.N.ZDU), and in compliance with Directive 2010/63/EU. C57BL/6J mice were housed under controlled environmental conditions (23 ± 1°C, 50 ± 5% relative humidity) on a 12 h light/dark cycle, with unrestricted access to food and water.

Cell culture

Primary hippocampal neurons were prepared from postnatal day 1 (P1) animals. Newborn mice were euthanized, and both hippocampi were dissected in DPBS containing D-glucose (6.5 mg mL^{-1}; Gibco, Thermo Fisher Scientific, Waltham, MA, USA; #14190-094). Neuronal dissociation was carried out through enzymatic digestion followed by mechanical trituration, as previously described [16]. Cells were initially plated in high-glucose DMEM (Gibco, Thermo Fisher Scientific; #21063-029) supplemented with 10% fetal bovine serum (FBS; Gibco; #10270-106), 100 IU mL^{-1} penicillin, 100 µg mL^{-1} streptomycin (Gibco; #15140-122), and 2 mM Glutamax (Gibco; #35050-038). Cells were seeded in µ-Slide (IBIDI, #80106) (140,000 cells) or on coverslip (Sarstedt, #83.1840.002) (55,000 cells) pre-coated with poly-L-lysine (PLL, 10 µg mL^{-1}; Sigma-Aldrich, #P4707). After 4 h, the culture medium was replaced with Neurobasal-A medium (Gibco; #12348-017) supplemented with B27 (Gibco; #17504-044), 2 mM Glutamax, 50 IU mL^{-1} penicillin, 50 µg mL^{-1} streptomycin, and 2.5 µM cytosine β-D-arabinofuranoside (AraC; Sigma-Aldrich; #C1768).

Rat pheochromocytoma PC12 cells (ATCC, Manassas, VA, USA, passage 6-12) were maintained in Dulbecco's modified Eagle's medium supplemented with 10% horse serum, 5% FBS, 100 IU mL^{-1} penicillin, 100 µg mL^{-1} streptomycin, and 2 mM L-Glutamax. To induce differentiation, PC12 cells were cultured in serum-reduced medium (1% FBS) supplemented with NGF 100 ng mL^{-1} (Sigma-Aldrich, #N5415). Experiments were conducted in PLL-coated Petri dishes (35 mm) or coverslip at cell density of 2.5×10^4 cells cm^{-2}.

Cells were maintained at 37°C in a humidified atmosphere containing 5% CO_2.

Drug treatment

Neurons were seeded at DIV0 and cultured in cell culture medium until DIV1. At DIV1, the medium was supplemented with Nocodazole 1.8 ng mL^{-1} (Sigma-Aldrich, Burlington, Massachusetts, US, #SML1665) until DIV6.

Magnetic nanoparticles (MNPs)

Commercial MNPs are magnetite nanoparticles (Fluid-MAG-ARA, Chemicell, Germany; #4115) characterized by a core of iron oxide (approximately 75±10 nm in diameter) and an outer layer of glucoronic acid. The hydrodynamic diameter is 100 nm. The saturation mass magnetization of 59 A m^2

kg^{-1}, as stated from the supplier. The standard working concentration of MNPs in experiments was 5 µg mL^{-1}.

Home-made MNPs were synthesized with minor modifications to a previously described protocol [26]. Briefly, 2.36 g of $FeCl_3 \cdot 6H_2O$ (Sigma-Aldrich, #44944) was dissolved in 40 mL of sterile Milli-Q water, followed by the addition of 0.86 g of $FeCl_2 \cdot 4H_2O$ (Sigma-Aldrich, #44939) with continuous stirring until complete dissolution. The solution was heated to 90°C, and 30% NH_4OH (Sigma-Aldrich, #221228) was gradually added at a slow, constant flow rate. After a 2-hour boiling period, magnetic particles were isolated using a Neodymium-Iron-Boron (Nd-FeB) magnet (15-39 mm). Residual impurities were removed by incubating the particles with 2M HNO_3 (Sigma-Aldrich, #84378) for 5 minutes, followed by five washing steps with Milli-Q water, each employing magnetic separation for 5 minutes. The purified nanoparticles were stored at 4°C. Iron concentration was determined via a thiocyanate assay, as previously described.[19] The standard working concentration of MNPs in experiments was 3.7 µg mL^{-1}.

Magnetic properties and characterization of MNPs

The magnetic properties of the samples were evaluated at T=6K and 325K with a commercial superconducting quantum interference device magnetometer (SQUID, MPMS Quantum Design®) in the -5 T< H < 5 T range. The crystalline structure, morphology and size dispersion of the MNPs were analysed by transmission electron microscopy (TEM) and high-resolution TEM (HRTEM) with Tecnai T20 (ThermoFisher Scientific) microscope operating at 200 kV at room temperature (RT). Size distribution of MNPs were derived from TEM images.

MNP Uptake and Degradation Assessment

To assess the degradation rate, cellular lysates were collected from $0.5 \cdot 10^6$ cells at various time points, and the amount of released iron was quantified according to the manufacturer's protocol (Bioassay Systems, DIFE-250).

Plasmids

The plasmid pet21α:His6:mEGFP:ΔNMms6 was kindly provided by Prof. Dr. J. Piehler (Biophysics, University of Osnabrück, Germany). Additionally, an expression plasmid encoding a membrane-interacting protein was designed to target the nanoparticles specifically. The plasmid Lck-GFP:Mms6 was constructed by subcloning the Mms6 domain (Genewiz, Germany) into the Lck-EGFP plasmid (Addgene, #61099). For compatibility with mammalian expression systems, the coding sequences of both fusion proteins were subsequently cloned into the pcDNA3.1 backbone by restriction digestion. Transformed bacteria were streaked onto agar plates containing the appropriate antibiotic. Plasmid DNA was amplified and isolated using a kit (Macherey-Nagel, #740412).

Recombinant protein expression

For bacterial expression, *E. coli* Rosetta DE3pLys cells were transformed with plasmid DNA encoding the protein of interest. Single colonies were cultured overnight (ON) in selective LB medium, followed by expansion at 37°C with vigorous shaking. Protein expression was induced at an OD600 of 0.5-0.6 by adding 0.5 mM IPTG (Merck KGaA, #15502) and incubating ON at 16-18°C. Cells were harvested by centrifugation at 4°C (4500×*g*, 45 min) and resuspended in freshly prepared lysis buffer containing protease inhibitors, PMSF, and glycerol. For denaturing conditions, buffers were prepared according to the manufacturer's guidelines (Thermo Fisher Scientific, #88221) with minor adjustments. Cell lysis was carried out via tip sonication (7 min, 50% duty cycle). The lysate was treated with 1% Triton X-100 (Merck, #T8787) and lysozyme (Sigma-Aldrich, #L-2879, 100 µg mL^{-1}), incubated on ice, stored ON at -80°C, and subsequently sonicated again (10 s, 100% duty cycle). Insoluble materials were removed by centrifugation (4°C, 20,000×*g*, 45 min). His-tagged proteins were purified using HisPur™ Ni-NTA Resin (Thermo Fisher Scientific, #88221) and concentrated via ultrafiltration (Centricon Plus, 10 kDa cutoff, #UFC701008). The final protein aliquots were stored at -80°C in dilution buffer (30 mM HEPES, 150 mM KCl, pH 7.5).

Protein Analysis

Purified proteins were analyzed for purity and integrity by SDS-PAGE, followed by Coomassie staining. Electrophoresis was performed on 12% Tris-glycine gels using a Mini-PROTEAN chamber (Bio-Rad). For Western blotting, proteins were transferred to nitrocellulose membranes (Amersham, #1060003)) using the Trans-Blot Turbo Transfer System (Bio-Rad). Dot blot analysis was performed by directly spotting samples onto membranes. Membranes were blocked with BSA (Sigma-Aldrich, #A7906) in PBS-Tween (Sigma-Aldrich, #P1379, 0.05%) and incubated ON at 4°C with primary antibodies (anti-GFP, 1:1000, Merck, #6539). After washing, membranes were incubated with secondary antibodies (anti-mouse IgG HRP, 1:5000-10,000, Merck, #A9044) for 1 hour at RT. Protein detection was achieved via enhanced chemiluminescence (Clarity Max™ Western ECL Substrate, Bio-Rad, #1705060), and signals were visualized using a ChemiDoc™ Molecular Imager (Bio-Rad). Recombinant protein concentration was determined using the BCA assay (ThermoFisher, #23225).

Biofunctionalization of MNPs

Recombinant proteins were conjugated to bare MNPs via the iron-binding properties of the ΔNMms6 domain [3-5]. Fusion proteins were thawed, washed, and resuspended in Milli-Q water. They were then incubated ON with sonicated MNPs (10 minutes, 15000×*g*, 4°C) at a 1:20 protein-to-MNP molar ratio. After incubation, the complexes were washed three times with sterile water to remove unbound protein and uncoated nanoparticles, then resuspended in sterile water and stored at 4°C. Protein binding and hydrodynamic diameter was measured using Dynamic Light Scattering (DLS), Zeta potential with a Zetasizer Nano-ZS (Malvern Panalytical) at 25°C. Conjugation efficiency was assessed by Blot analysis (instrument). FTIR spectroscopy was employed to investigate molecular interactions during in the samples of MNPs before and after the conjugation protocol. FTIR spectra were obtained using a Bruker VERTEX 70v Shimadzu IRAffinity-1 spectrophotometer (4000-600 cm^{-1}) using Attenuated Total

Reflectance Fourier Transform Infrared spectroscopy (ATR FT-IR) with samples either dried on polystyrene films or applied directly to the detection chamber.

Protein Localization

For protein localization studies, transfections were conducted using Lipofectamine 2000 following the supplier's instructions Invitrogen, #11668). Differential fluorescence analysis was performed using ImageJ software, employing the "Plot Profile" function. The images analyzed in this study, acquired by confocal microscopy, represent a central Z stack. Specifically, the ratio between the mean fluorescence at the membrane level (considering a thickness of 1 µm for each of the two sides of the cell) and that at the cytoplasmic level (considering the intermediate thickness between the two membrane sides) was calculated.

Nano-pulling assay

Cell growth medium was modified with MNPs four hours after seeding. The magnetic field (stretch group) or a null magnetic field (control group) was applied from DIV1 (if not stated differently). To generate an axial force, a bridge magnetic applicator was used, which provided a constant magnetic field gradient of 20 T m^{-1}, as previously validated (Figure S1).[20] To generate a radial force, a Halbach-like cylinder magnetic applicator was used, which provided a magnetic field gradient in the range of 22±5 T m^{-1} in the radial direction outwards (Figure S4).). The magnetic fields and their spatial derivatives were determined by a 3D finite element simulation (COMSOL Multiphysics 6.2).

Cell transduction, time-lapse imaging and data analysis

At DIV1, cells were transduced with a doxycycline-inducible EB3 lentiviral vector Inducible expression of RFP-EB3 was chosen to avoid construct overexpression. The lentiviral vector was generated cloning the RFP-EB3 sequence (from pTagRFP-EB3 vector, Evrogen #FP365, kindly provided by Ilaria Tonazzini, CNR-NANO, Pisa, Italy) into a third generation Tet-on lentiviral vector (from Prof. Dr. I. Barde, CNSR, France). Lentiviral particles were produced by the Viral Core Facility, Charité – Universitätsmedizin Berlin. Cells were transduced with $5{\cdot}10^5$ particles·ml^{-1} and 4 ug ml^{-1} of polybrene. Doxycycline at 0.25 µg·ml^{-1} concentration was added at DIV3 to yield mid-level RFP-EB3 expression. Live imaging was performed using an LSM 900 Airyscan microscope (Zeiss) in super-resolution mode, equipped with a Plan-Apochromat 63×/1.40 Oil DIC M27 objective and an environmental incubation chamber maintained at 37 °C and 5% CO_2. A variable digital magnification ranging from 4× to 6× was applied, allowing the acquisition of fields of view of approximately 500 × 175 pixels (24.5 × 8.5 µm).

EB3 comets were imaged inside the microchannels using a 561-nm laser line set to 0.7% power, with a digital gain of 1, a scan speed of 7, and 4× line averaging. Time-lapse images of RFP-EB3 dynamics in transduced cells were acquired at 2 s frame time, for a total of 60 frames per video. Each sample was imaged for approximately 2 h.

The analysis of EB3 comet dynamics was carried out using Fiji. For each video, ROIs were manually traced along the trajectories. Kymographs were generated from each video using the *Multi* Kymograph plugin and subsequently analyzed with the *KymoAnalyzer* plugin.[51] Specifically, the Tracks function was used to identify and trace individual comets within each kymograph. The *CargoPopulation*, *NetCargoPopulation*, and *Segments functions* were employed to extract quantitative information regarding the number of comets, movement segments, directionality, velocity and pause frequency of each individual comet. The software categorized comets as anterograde, retrograde, oscillating, and stalled. Unless otherwise specified, "comets" refers to the entire population. *NetVelocity*, *NetCargoPopulation*, and S*plitPauseFrequencyPerSec* folders were considered for the analysis. A velocity cut-off of 0.01 $\mu m \cdot s^{-1}$ was manually applied for both the anterograde and retrograde velocity groups. For the ROIs of the axon and the GCs, the Huang automatic thresholding method was used to determine the area for the *NetCargoPopulation* analysis.

Immunohistochemistry (HIC) and imaging

Cells were fixed in 2% PFA for 10 minutes at RT and permeabilized in 0.5% Triton X-100 for 10 minutes at RT. Samples were then blocked in 5% serum, 0.3% Triton X-100 in DPBS for 1 hour at RT. Samples were incubated ON at 4°C with primary antibodies were diluted in 3% serum, 0.2% Triton X-100 in DPBS (TUBBIII, Sigma-Aldrich, Burlington, Massachusetts, US, #T8578, 1:500; acetylated TUBA, Sigma-Aldrich, Massachusetts, US, #T7451, 1:400; tyrosinated TUBA, Abcam, # ab6160, 1:400; Poly-E, Adipogen, #IN105, 1:500; Poly-glutamylation Modification, Adipogen, #GT335, 1:500; anti-GFP, Thermo Fisher, #A6455, 1:500). After ON incubation at 4°C, samples were washed and then incubated with secondary antibodies (Thermo Fisher Scientific, Waltham, Massachusetts, US, #O6380, #A32731, #A11011, #A32728, #R6393, #A21449, 1:500; Abcam, Cambridge, UK, #ab150169, 1:500) and Hoechst 33342 (Thermo Fisher Scientific, #H3570, 1:1000) for 1 hour at RT.

Samples were imaged with a laser scanning confocal microscope (Nikon AX, Eclipse Ti2 inverted microscope). Images were acquired with a 60× objective oil immersion (PLAN APO λD 60x OIL OFN25 DIC N2) or 20× (PLAN APO λD 20x OFN25 DIC N2). Images were acquired at 1024 × 1024 or 2048 × 2048 pixel resolution with a 2× or 4× averaging. Images were acquired using a 405 nm laser (425-475 nm emission filter) or a 488 nm laser (500-550 nm emission filter) or a 561 laser (570-620 nm emission filter) or a 640 nm laser (663-738 nm emission filter). Gain and exposure time varied for the specific experiments and the related metadata are available in the original *.nd2* image files

Toxicity Assessment

Dose-response assays were performed to evaluate the potential toxicity of MNPs and recombinant proteins. After seeding 30,000 cells on a coated 48-well plate, cells were treated with varying concentrations of MNPs/proteins. At DIV3, cells were fixed, and the standard immunohistochemistry protocol was applied. Cell density was assessed by counting viable cells TUBBIII positive neurons.

Image analysis of cell morphology

NeuronJ, a Fiji plugin, was used to evaluate axon length. Briefly, non-interconnected primary axons (TUBBIII stained) were traced with the tracing tool and were analyzed from 10× magnification images (cut-off 50 μm).

Cell morphological analysis was performed using Neurolucida Explorer (Neurolucida®360, mbf Bioscience). In particular, the Structure Analysis function was used to extract morphometric parameters related to the soma and cellular processes. Soma area and roundness were measured, while dendrites and axons were analyzed in terms of total length, area, volume, and spatial orientation.

Image analysis of fluorescence

For fluorescence quantification, we evaluated the total fluorescence and/or the mean fluorescence ( ), where *IntDen* is the integrated density (defined as the sum of all the pixel intensities in that selected region), *A* is the area of the ROI and is the mean fluorescence of background readings.

The ratio of acetylated versus tyrosinated TUBA or poly-E versus TUBBIII or poly-glut vs TUBBIII or poly-glut vs poly-E was determined from total fluorescence (*f*) intensities.

Statistical analysis

Data were analysed and plotted using GraphPad 10. Results are presented as scatter plot (mean ± the standard error of the mean (SEM)) or data distribution (violin plot). The Kolmogorov-Smirnov (KS) normality test was employed to assess data distribution normality. GraphPad was used to detect and remove outliers. For data following a normal distribution, unpaired t-tests and ANOVA were used, whereas for non-normally distributed data, the Mann-Whitney U test or Kruskal-Wallis test was performed. Statistical significance was set at $p \leq 0.05$.

Sample size was calculated using G*Power ($\alpha = 0.05$, power=0.8), resulting in n = 120 axons for axon length (effect size: 0.35), n = 60 axons / images for MT PTM and protein localization (effect size: 0.5), and n = 25 axons for EB3 comets (effect size = 0.8). These axons were derived from four biological replicates and from five biological replicates for EB3 live-imaging. For morphological analysis we analysed n = 200 axons, n = 180 somata and n = 340 dendrites derived for four replicates (10 images per replicate). The analysis of 40 images was required to have the total sample size N=120 required for the orientation-dependent analysis ($\alpha = 0.05$, power=0.8, effect size = 0.3). Data reported for MNP characterization (Figure 3) are related to three replicates.

Declarations

Acknowledgment

The study was supported by the Italian Fund for Science (FIS) (call FIS2, NEMESIS project) and the Human Frontier Science Program (RGP0026/2021). The authors thank Nicole Bertola for the support given in MNP synthesis and validation.

Competing interests

The authors declare no competing interests.

Author contributions. Analysis of neuron morphology, MT PTMs, and MT dynamics was performed by L.D.P. T.J.N.S. conducted the synthesis and chemical and biological validation of the functionalized MNPs. A.C. and L.M. contributed to the EB3 experiments. F.S. performed the Neurolucida analysis. E.L. contributed to molecular cloning. M.C. contributed to protein localization studies. P.B. conducted the magnetic applicator design and FEM simulations. J.A.F.G. and G.F.G. contributed to the physical characterization of the functionalized MNPs. V.R. designed the experiments, analyzed the data, and wrote the paper. The manuscript was revised and approved by all authors.

References

1. Raffa, V. Force: A messenger of axon outgrowth. *Semin. Cell Dev. Biol.* **140**, 3–12 (2023).
2. del Rio, A. *et al.* Stretching Single Talin Rod Molecules Activates Vinculin Binding. *Science (1979).* **323**, 638–641 (2009).
3. Hirata, H., Tatsumi, H., Lim, C. T. & Sokabe, M. Force-dependent vinculin binding to talin in live cells: a crucial step in anchoring the actin cytoskeleton to focal adhesions. *American Journal of Physiology-Cell Physiology* **306**, C607–C620 (2014).
4. Rognoni, L., Stigler, J., Pelz, B., Ylanne, J. & Rief, M. Dynamic force sensing of filamin revealed in single-molecule experiments. *Proceedings of the National Academy of Sciences* **109**, 19679–19684 (2012).
5. Zhou, J. *et al.* Mechanism of Focal Adhesion Kinase Mechanosensing. *PLoS Comput. Biol.* **11**, e1004593 (2015).
6. Kong, F., García, A. J., Mould, A. P., Humphries, M. J. & Zhu, C. Demonstration of catch bonds between an integrin and its ligand. *Journal of Cell Biology* **185**, 1275–1284 (2009).
7. Wu, J., Goyal, R. & Grandl, J. Localized force application reveals mechanically sensitive domains of Piezo1. *Nat. Commun.* **7**, 12939 (2016).
8. Falleroni, F. *et al.* Mechanotransduction in hippocampal neurons operates under localized low picoNewton forces. *iScience* **25**, 103807 (2022).
9. Brouhard, G. J. & Rice, L. M. Microtubule dynamics: an interplay of biochemistry and mechanics. *Nat. Rev. Mol. Cell Biol.* **19**, 451–463 (2018).
10. Tilney, L. G. *et al.* MICROTUBULES: EVIDENCE FOR 13 PROTOFILAMENTS. *J. Cell Biol.* **59**, 267–275 (1973).
11. Mitchison, T. & Kirschner, M. Dynamic instability of microtubule growth. *Nature* **312**, 237–242 (1984).
12. Desai, A. & Mitchison, T. J. MICROTUBULE POLYMERIZATION DYNAMICS. *Annu. Rev. Cell Dev. Biol.* **13**, 83–117 (1997).

13. Jánosi, I. M., Chrétien, D. & Flyvbjerg, H. Structural Microtubule Cap: Stability, Catastrophe, Rescue, andThird State. *Biophys. J.* **83**, 1317–1330 (2002).
14. Gudimchuk, N. B. *et al.* Mechanisms of microtubule dynamics and force generation examined with computational modeling and electron cryotomography. *Nat. Commun.* **11**, 3765 (2020).
15. Franck, A. D. *et al.* Tension applied through the Dam1 complex promotes microtubule elongation providing a direct mechanism for length control in mitosis. *Nat. Cell Biol.* **9**, 832–837 (2007).
16. de Vincentiis, S. *et al.* Extremely Low Forces Induce Extreme Axon Growth. *Journal of Neuroscience* https://doi.org/10.1523/JNEUROSCI.3075-19.2020 (2020) doi:10.1523/JNEUROSCI.3075-19.2020.
17. Falconieri, A. *et al.* Axonal plasticity in response to active forces generated through magnetic nano-pulling. *Cell Rep.* **42**, 111912 (2023).
18. Baas, P. W., Deitch, J. S., Black, M. M. & Banker, G. A. Polarity orientation of microtubules in hippocampal neurons: uniformity in the axon and nonuniformity in the dendrite. *Proceedings of the National Academy of Sciences* **85**, 8335–8339 (1988).
19. Raffa, V. *et al.* Piconewton Mechanical Forces Promote Neurite Growth. *Biophys. J.* **115**, 2026–2033 (2018).
20. De Vincentiis, S. *et al.* 3D-printed weight holders design and testing in mouse models of spinal cord injury. *Frontiers in Drug Delivery* **4**, (2024).
21. Jacques-Fricke, B. T., Seow, Y., Gottlieb, P. A., Sachs, F. & Gomez, T. M. Ca $^{2+}$ Influx through Mechanosensitive Channels Inhibits Neurite Outgrowth in Opposition to Other Influx Pathways and Release from Intracellular Stores. *The Journal of Neuroscience* **26**, 5656–5664 (2006).
22. Ranade, S. S., Syeda, R. & Patapoutian, A. Mechanically Activated Ion Channels. *Neuron* **87**, 1162–1179 (2015).
23. Staniland, S. S. & Rawlings, A. E. Crystallizing the function of the magnetosome membrane mineralization protein Mms6. *Biochem. Soc. Trans.* **44**, 883–890 (2016).
24. Shipunova, V. O. *et al.* Self-assembling nanoparticles biofunctionalized with magnetite-binding protein for the targeted delivery to HER2/neu overexpressing cancer cells. *J. Magn. Magn. Mater.* **469**, 450–455 (2019).
25. Benediktsson, A. M., Schachtele, S. J., Green, S. H. & Dailey, M. E. Ballistic labeling and dynamic imaging of astrocytes in organotypic hippocampal slice cultures. *J. Neurosci. Methods* **141**, 41–53 (2005).
26. Shipunova, V. O. *et al.* Data on characterization of magnetic nanoparticles stabilized with fusion protein of Barstar and C-term part of Mms6. *Data Brief* **21**, 1659–1663 (2018).
27. Moutin, M., Bosc, C., Peris, L. & Andrieux, A. Tubulin post-translational modifications control neuronal development and functions. *Dev. Neurobiol.* **81**, 253–272 (2021).
28. Portran, D., Schaedel, L., Xu, Z., Théry, M. & Nachury, M. V. Tubulin acetylation protects long-lived microtubules against mechanical ageing. *Nat. Cell Biol.* **19**, 391–398 (2017).

29. Torrino, S. *et al.* Mechano-induced cell metabolism promotes microtubule glutamylation to force metastasis. *Cell Metab.* **33**, 1342-1357.e10 (2021).
30. Kerr, J. P. *et al.* Detyrosinated microtubules modulate mechanotransduction in heart and skeletal muscle. *Nat. Commun.* **6**, 8526 (2015).
31. Witte, H., Neukirchen, D. & Bradke, F. Microtubule stabilization specifies initial neuronal polarization. *J. Cell Biol.* **180**, 619–632 (2008).
32. Falconieri, A. *et al.* The Extremely Low Mechanical Force Generated by Nano-Pulling Induces Global Changes in the Microtubule Network, Nuclear Morphology, and Chromatin Transcription in Neurons. *Small* **21**, (2025).
33. Zhang, X. *et al.* The distinct initiation sites and processing activities of TTLL4 and TTLL7 in glutamylation of brain tubulin. *Journal of Biological Chemistry* **299**, 104923 (2023).
34. Bodakuntla, S. *et al.* Tubulin polyglutamylation is a general traffic-control mechanism in hippocampal neurons. *J. Cell Sci.* **133**, (2020).
35. Shimada, T. *et al.* Shootin1 interacts with actin retrograde flow and L1-CAM to promote axon outgrowth. *Journal of Cell Biology* **181**, 817–829 (2008).
36. Woo, S. & Gomez, T. M. Rac1 and RhoA promote neurite outgrowth through formation and stabilization of growth cone point contacts. *Journal of Neuroscience* https://doi.org/10.1523/JNEUROSCI.4209-05.2006 (2006) doi:10.1523/JNEUROSCI.4209-05.2006.
37. Myers, J. P. & Gomez, T. M. Focal adhesion kinase promotes integrin adhesion dynamics necessary for chemotropic turning of nerve growth cones. *Journal of Neuroscience* https://doi.org/10.1523/JNEUROSCI.2381-11.2011 (2011) doi:10.1523/JNEUROSCI.2381-11.2011.
38. Turney, S. G. *et al.* Nerve growth factor stimulates axon outgrowth through negative regulation of growth cone actomyosin restraint of microtubule advance. *Mol. Biol. Cell* https://doi.org/10.1091/mbc.E15-09-0636 (2016) doi:10.1091/mbc.E15-09-0636.
39. Lamoureux, P., Buxbaum, R. E. & Heidemann, S. R. Direct evidence that growth cones pull. *Nature* https://doi.org/10.1038/340159a0 (1989) doi:10.1038/340159a0.
40. Lee, A. C. & Suter, D. M. Quantitative analysis of microtubule dynamics during adhesion-mediated growth cone guidance. *Dev. Neurobiol.* **68**, 1363–1377 (2008).
41. Athamneh, A. I. M. *et al.* Neurite elongation is highly correlated with bulk forward translocation of microtubules. *Sci. Rep.* **7**, 7292 (2017).
42. Biswas, S. & Kalil, K. The Microtubule-Associated Protein Tau Mediates the Organization of Microtubules and Their Dynamic Exploration of Actin-Rich Lamellipodia and Filopodia of Cortical Growth Cones. *The Journal of Neuroscience* **38**, 291–307 (2018).
43. Suter, D. M., Errante, L. D., Belotserkovsky, V. & Forscher, P. The Ig Superfamily Cell Adhesion Molecule, apCAM, Mediates Growth Cone Steering by Substrate–Cytoskeletal Coupling. *Journal of Cell Biology* **141**, 227–240 (1998).

44. Miles, L., Powell, J., Kozak, C. & Song, Y. Mechanosensitive Ion Channels, Axonal Growth, and Regeneration. *The Neuroscientist* **29**, 421–444 (2023).
45. Kim, T. & Chang, S. Quantitative Evaluation of the Mode of Microtubule Transport in Xenopus Neurons. *Mol. Cells* **21**, 76–81 (2006).
46. Peris, L. *et al.* Motor-dependent microtubule disassembly driven by tubulin tyrosination. *Journal of Cell Biology* **185**, 1159–1166 (2009).
47. Janke, C. & Montagnac, G. Causes and Consequences of Microtubule Acetylation. *Current Biology* **27**, R1287–R1292 (2017).
48. Xu, Z. *et al.* Microtubules acquire resistance from mechanical breakage through intralumenal acetylation. *Science (1979).* **356**, 328–332 (2017).
49. de Rooij, R., Kuhl, E. & Miller, K. E. Modeling the Axon as an Active Partner with the Growth Cone in Axonal Elongation. *Biophys. J.* **115**, 1783–1795 (2018).
50. Miller, K. E. & Suter, D. M. An Integrated Cytoskeletal Model of Neurite Outgrowth. *Front. Cell. Neurosci.* **12**, (2018).
51. Neumann, S., Chassefeyre, R., Campbell, G. E. & Encalada, S. E. <scp>KymoAnalyzer</scp>: a software tool for the quantitative analysis of intracellular transport in neurons. *Traffic* **18**, 71–88 (2017).

Figures

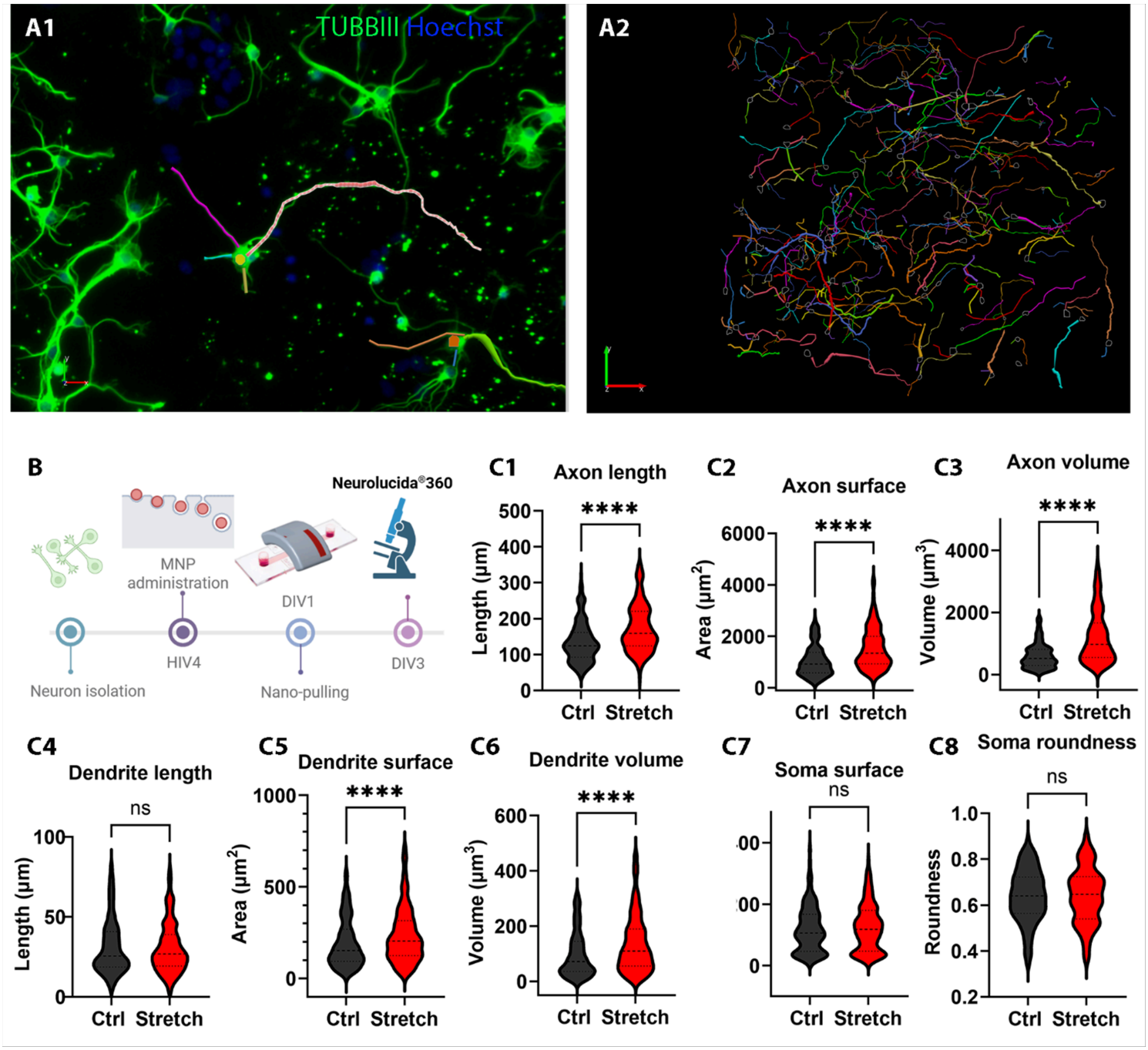

Figure 1

Morphological analysis of stretched hippocampal neurons via Neurolucida 360. A1-2) Automatic tracing of neuronal structures . "Soma" function was used to identify somata and the "Tree" function to trace dendrites and axons. B) Loading protocol of hippocampal neurons with MNPs. MNPs are added in cell growth media at the concentration of 5 µg mL^{-1} four hours after cell seeding (hours in vitro, HIV4) and the magnet is applied from day in vitro (DIV)1. Neurons are stretched for the subsequent 48 h (if not indicated differently). Created in https://BioRender.com. C1) Axon length (violin plot). Mann Whitney test, p < 0.0001, Mann-Whitney U=13047. C2) Axon surface (violin plot). Mann Whitney test, p < 0.0001, Mann-Whitney U=11416. C3) Axon volume (violin plot). Mann Whitney test, p < 0.0001, Mann-Whitney U=8735. In C1-3, n=200 axons from four replicates. C4) Dendrite length (violin plot). Mann Whitney test, p=0.94,

Mann-Whitney U=49897. C5) Dendrite surface (violin plot). Mann Whitney test, p < 0.0001, Mann-Whitney U=39987. C6) Dendrite volume (violin plot). Mann Whitney test, p < 0.0001, Mann-Whitney U=33547. In C4-6, n=340 dendrites from four replicates. C7) Soma surface (violin plot). Mann Whitney test, p = 0.46, Mann-Whitney U=15383. C8) Soma roundness (violin plot). t-test, p=0.95, t=0.057, df=357. In C7-8, n = 180 somata from four replicates.

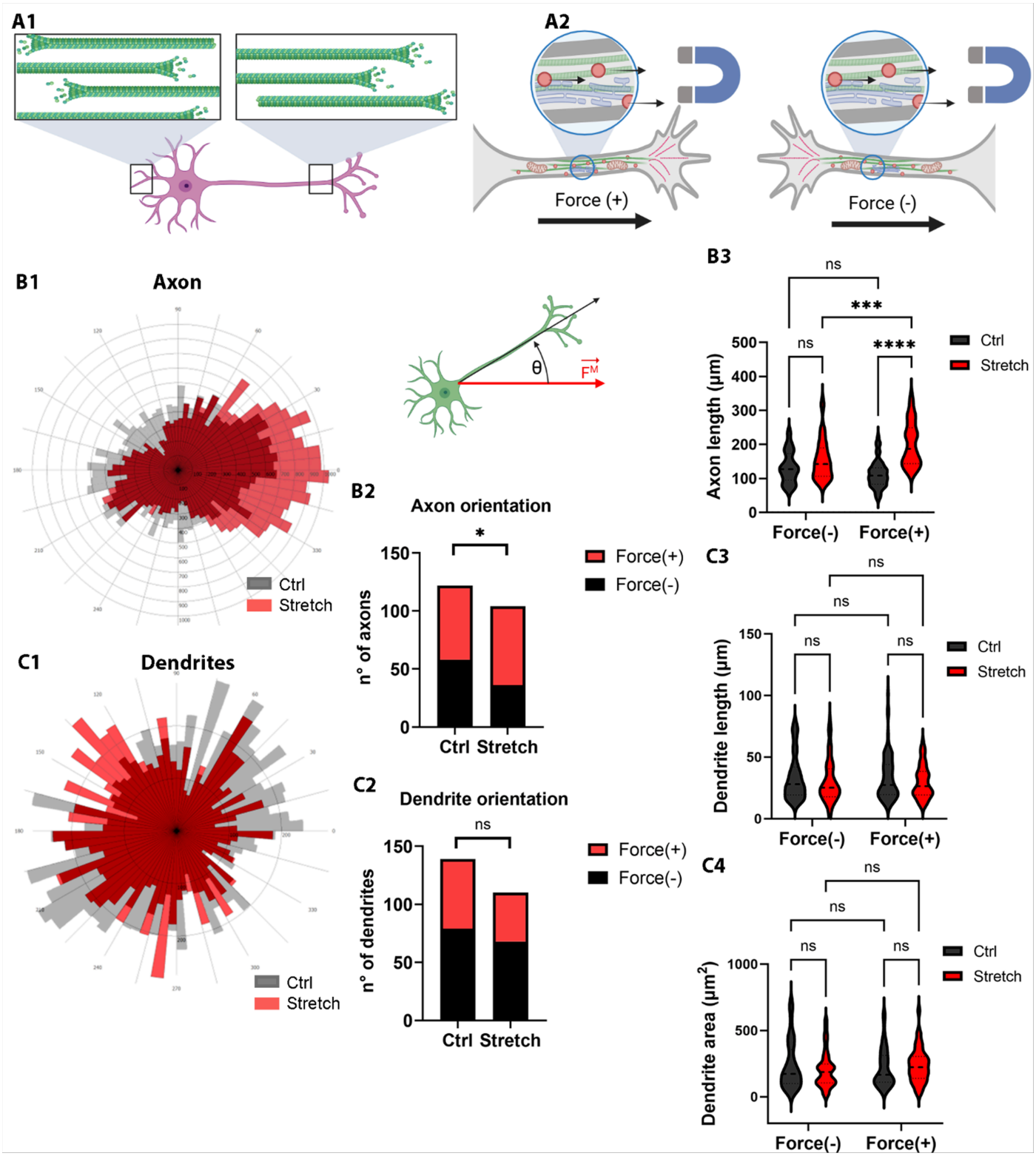

Figure 2

Nano-pulling is orientation-dependent. A1) In axons, microtubules have their (+) end preferentially oriented from soma to tip, whereas in dendrites they have a mixed orientation. A2) Hereafter, force (+) refers to a magnetic force with the radial component in the soma-to-tip orientation, while force (-) refers to a magnetic force with the radial component in the tip-to-soma orientation. Created in https://BioRender.com. B1) Polar histograms of axon length (360° < θ < 0°), n=281 axons (Ctrl), 212 axons (Stretch) taken from 10 pictures from 4 replicates. Kolmogorov-Smirnov test, p < 0.0001, Kolmogorov-Smirnov D=0.31. B2) Data from B1 have been plotted to show frequency distribution of axons with 330° <θ < 30° (force (+) group) and axons with 150° < θ < 210° (force (-) group). Chi square test, p = 0.013, Chi-square = 6.10. B3) Data from B2) have been plotted to show axon length (violin plot). Two-way ANOVA, Tukey's multiple comparisons test. Row factor (force orientation): p = 0.076. F (1, 217) = 3.18. Column factor (nano-pulling): p < 0.0001, F (1, 217) = 57.68. C1) Polar histograms of dendrite length (360°<θ<0°), n = 443 dendrites (Ctrl), 358 dendrites (Stretch) taken from 10 pictures from 4 replicates. Kolmogorov-Smirnov test, p = 0.88, Kolmogorov-Smirnov D = 0.042. C2) Data from C1 have been plotted to show frequency distribution of dendrites with 330° < θ < 30° (force (+) group) and axons with 150° < θ < 210° (force (-) group). Chi square test, p = 0.68, Chi-square = 0.17. C3) Data from C1 have been plotted to show dendrite length (violin plot). Two-way ANOVA, Tukey's multiple comparisons test. Row factor (force orientation): p = 0.99, F (1, 245) = 0.00034. Column factor (nano-pulling): p= 0.13, F (1, 245) = 2.36. C4) Data from experiments reported in C1 have been plotted to show dendrite surface (violin plot). Two-way ANOVA, Tukey's multiple comparisons test. Row factor (force orientation): p = 0.74, F (1, 231) = 0.11. Column factor (nano-pulling): p = 0.76, F (1, 231) = 0.093.

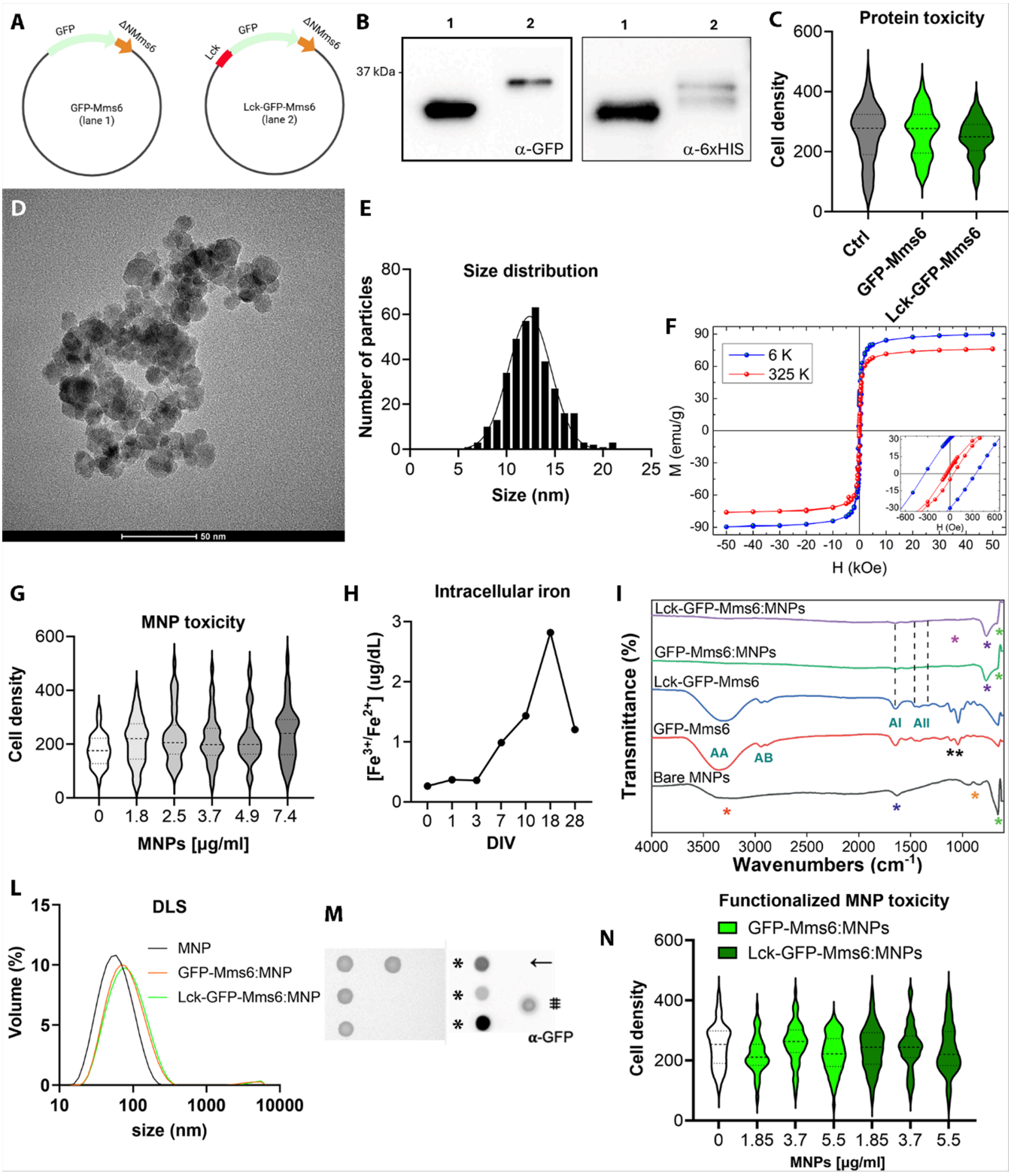

Figure 3

Design and validation of MNPs with or without a cell membrane localization signal. A) GFP-Mms6 and Lck-GFP-Mms6 constructs. Created in https://BioRender.com. B) Western Blot for anti-GFP (left) and for anti-6xHis (right). The detected bands correspond to the investigated POI. Lane 1 corresponds to GFP-Mms6 (31.2 kDa), lane 2 to Lck-GFP-Mms6 (36.6 kDa). C) Toxicity assay of the recombinant proteins. Cell density (number of TUBBIII- positive cells in 2.4 mm^2) of neurons incubated with the recombinant

proteins (GFP-Mms6 [0.023 mM]; Lck-GFP-Mms6 [0.004 mM] from DIV0 to DIV3. One-way ANOVA, Tukey's multiple comparisons test, n=60 images from 3 biological replicates, p = 0.55, F = 0.60. D) Transmission electron microscopy (TEM) images of bare MNPs revealed a spherical shape. E) Histogram of MNP size. Mean size of 12.4 ± 2.2 nm, based on measurements from 337 particles. R^2 = 0.97. F) Magnetization curve of bare iron oxide nanoparticles. Hysteresis curve evaluated at room temperature (n=3). G) Toxicity assay of the bare MNPs. Cell density (number of TUBBIII- positive cells in 2.4 mm^2) of neurons incubated with MNPs from DIV0 to DIV3. Kruskal-Wallis test, n = 60 images from 3 biological replicates, p = 0.14, Kruskal-Wallis statistic: 8.24. H) Intracellular iron concentration in hippocampal neurons at different timepoints. I) FTIR spectra of bare MNPs, functionalized MNPs and recombinant proteins. L) Dynamic light scattering of bare iron oxide nanoparticles. Size distribution by volume. M) Dot Blot analysis using anti-GFP antibody. On the left, colorimetric image of the blot; on the right, the corresponding chemiluminescence image. The "" indicates the functionalized MNPs (three replicates), the arrow indicates bare MNPs, and the "#" indicates the pure protein. N) Toxicity assay of the functionalized MNPs. Cell density (number of TUBBIII- positive cells in 2.4 mm^2) of neurons incubated with MNPs from DIV0 to DIV3. One-way ANOVA, Dunnett's multiple comparisons test, n = 60 images from 3 biological replicates, p = 0.04, F = 2.22. Comparison with control (0) is n.s. for all groups in C, G and N.*

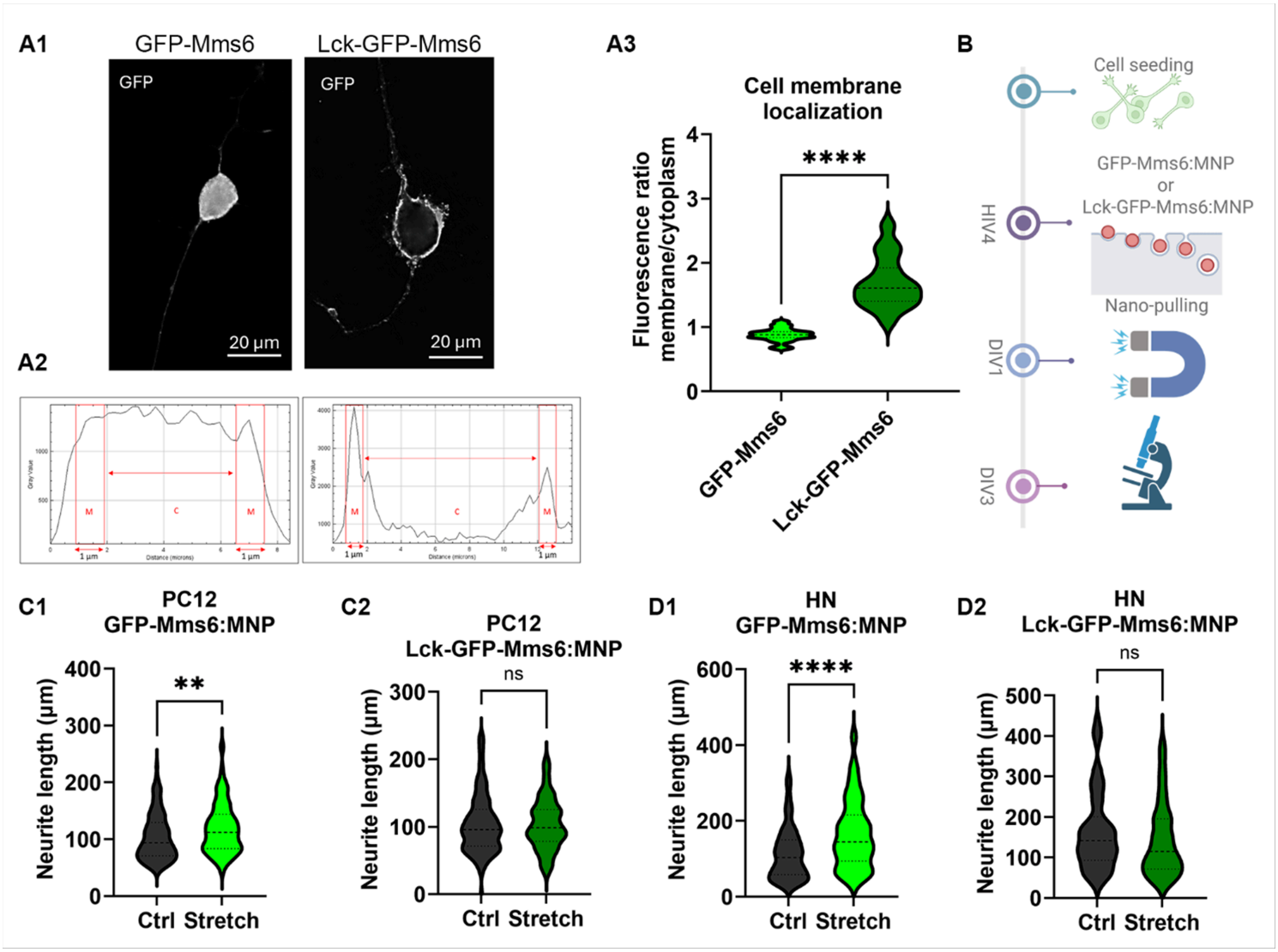

Figure 4

Nano-pulling does not occur with particles harboring a cell membrane localization domain. A1) Differential intracellular localization of GPF-Mms6 and Lck-GFP-Mms6 constructs in PC12 cells. A2) Plot profile of the fluorescence intensity. A3) Ratio between the fluorescence intensity in the cell membrane and cytoplasm. Violin plot, n = 60 cells, Mann Whitney test, p < 0.0001, Mann-Whitney U = 7. B) Timeline of the experiment. Created in https:./BioRender.com. C1) Stretch-growth assay in PC12 cells incubated with GFP-Mms6:MNP. Violin plot, n = 120 neurites, Mann Whitney test, p = 0.0046, Mann-Whitney U = 5474. C2) Stretch-growth assay in PC12 cells incubated with Lck-GFP-Mms6:MNP. Violin plot, n = 120 neurites, Mann Whitney test, p = 0.65, Mann-Whitney U = 6725. D1) Stretch-growth assay in hippocampal neurons (HN) incubated with GPF-Mms6:MNP. Violin plot, n = 120 neurites, Mann Whitney test, p < 0.0001, Mann-Whitney U=4565. D2) Stretch-growth assay in hippocampal neurons incubated with Lck-GPF-Mms6:MNP. Violin plot, n = 120 neurites, Mann Whitney test, p = 0.06, Mann-Whitney U = 6131.

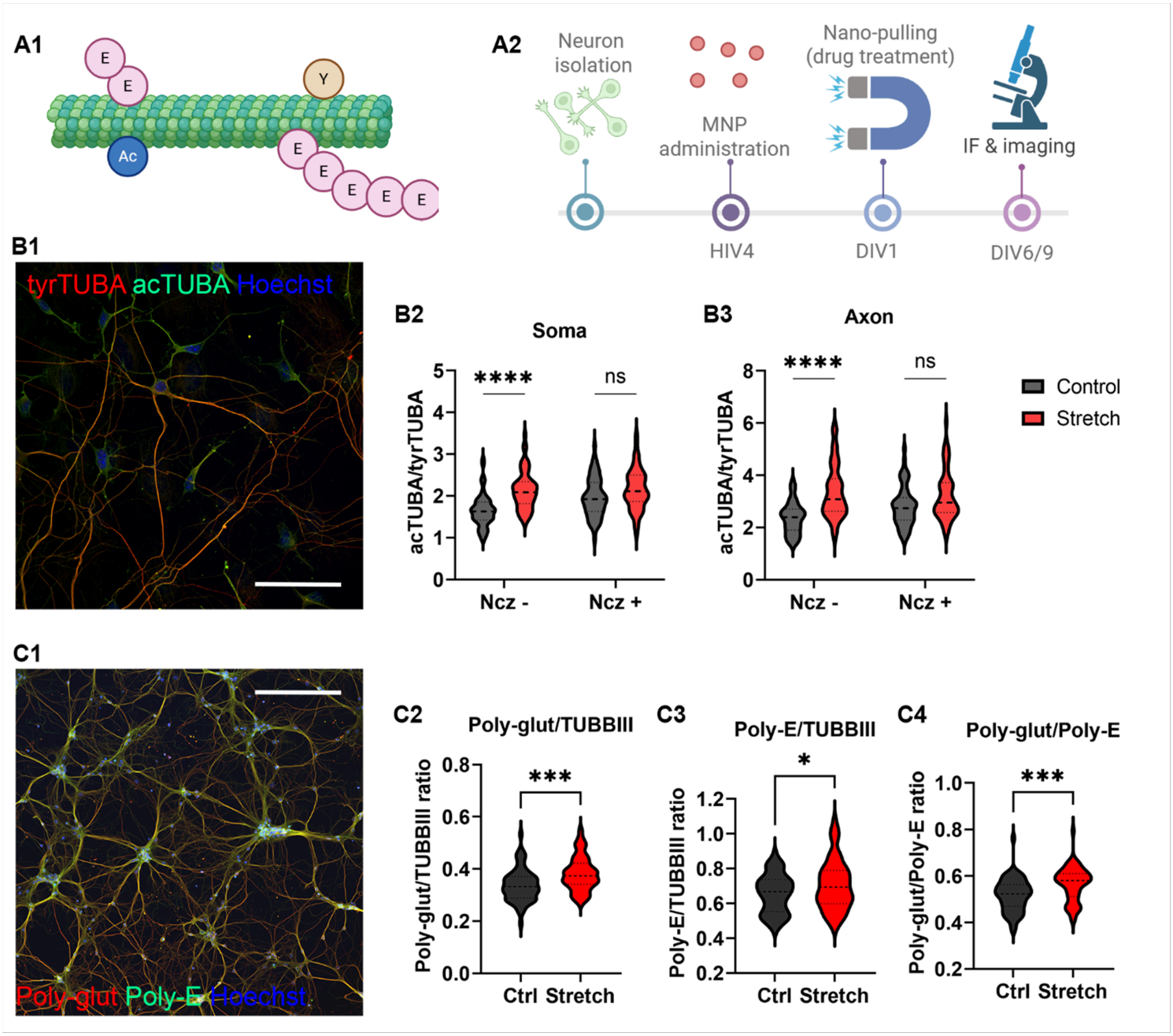

Figure 5

Microtubule post-translational modifications. A1) MT PTMs here considered are acetylation (ac), tyrosination (Y or tyr) and polyglutamylation (E). A2) MNPs are added in cell growth media at the concentration of 5 μg mL^{-1} four hours after cell seeding (HIV4) and the magnet is applied from DIV1. Neurons are stretched up to DIV6 for studying acTUBA/tyr TUBA and up to DIV9 for poly-glut/poly-E. B1) Immunofluorescence against acTUBA (green) and tyrTUBA (red) in control and stretched neurons at DIV6. Scale bars: 50 μm. B2) Ratio of acetylated versus tyrosinated α-tubulin in neuron somata. Violin plot, n = 60 axons from four replicates. Two-way ANOVA, Bonferroni multiple comparison test. Raw factor: nocodazole (Ncz) treatment, F (1, 233) = 8.66, p = 0.0036. Column factor: stretching, F (1, 233) = 34.12, p < 0.0001. B3) Ratio of acetylated versus tyrosinated α-tubulin in axons. Violin plot, n=60 axons from four replicates. Two-way ANOVA, Bonferroni multiple comparison test. Raw factor: nocodazole

(Ncz) treatment, F (1, 232) = 2.02, p = 0.16. Column factor: stretching, F (1, 232) = 42.15, p < 0.0001. C1) Immunofluorescence against poly-glut (red) and poli-E (green) in control and stretched neurons at DIV9. Scale bars: 50 µm. C2) Ratio of poly-glut versus TUBBIII in neuron network, n = 60 images from four replicates. t-test, two-tailed, t = 3.75, df = 111, p = 0.0003. C3) Ratio of poly-E versus TUBBIII in neuron network. n=60 images from four replicates. t-test, two-tailed, t = 2.06, df = 113, p = 0.041. C4) Ratio of poly-glut versus poly-E in neuron network. n=60 images from four replicates. Mann Whitney test, p = 0.0001, Mann-Whitney U=1016.

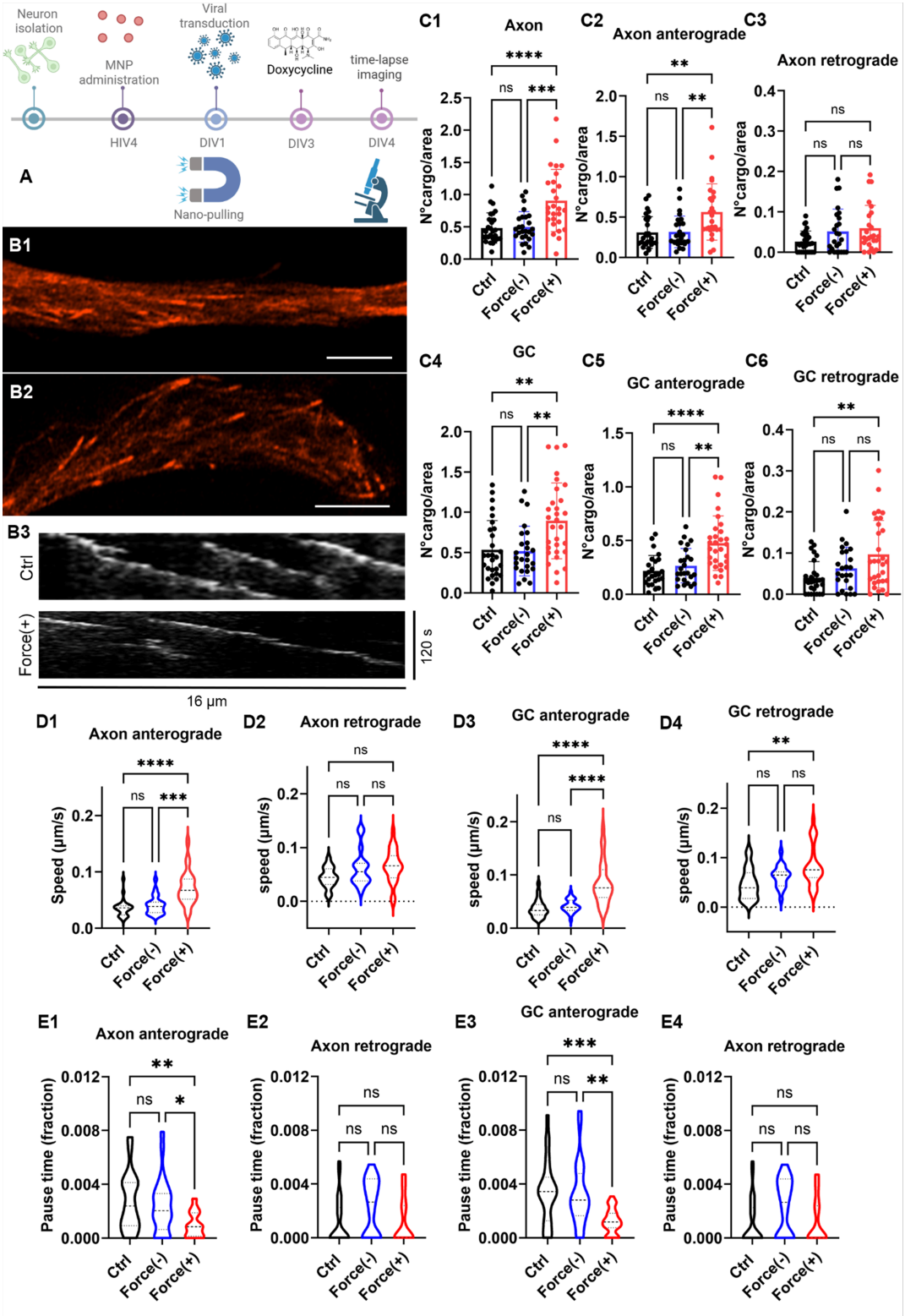

Figure 6

Tracking EB3 comets A) MNPs are added in cell growth media at the concentration of 5 µg mL^{-1} four hours after cell seeding (hours in vitro, HIV4), cells are infected at DIV1 and the magnet is applied after the removal of the transduction media, EB3 expression is induced at DIV3, analysis is performed at DIV4. B) Representative images of time-lapse acquisition of fluorescently-labelled EB3 comets in axon (B1, see supplementary video 1) and growth cone (B2, see supplementary video 2) Scale bar : 5 µm. B3) Example of kymographs. C1) Scatter plot of the density of the RFP-tagged EB3 comets in the axon (number per $µm^2$). One-way ANOVA, Tukey's multiple comparisons test, p < 0.0001, n = 26 axons. F = 13.52. C2) Scatter plot of the density of the RFP-tagged EB3 anterograde comets in the axon (number per $µm^2$). Kruskal-Wallis test, Dunn's multiple comparisons test, p = 0.0014, n = 26 axons. Kruskal-Wallis statistic = 13.16. C3) Scatter plot of the density of the RFP-tagged EB3 retrograde comets in the axon (number per $µm^2$). Kruskal-Wallis test, Dunn's multiple comparisons test, p = 0.073, n = 25 axons. Kruskal-Wallis statistic = 5.24. C4) Scatter plot of the density of the RFP-tagged EB3 comets in the GC (number per $µm^2$). Kruskal-Wallis test, Dunn's multiple comparisons test, p = 0.0012, n = 25 GCs, Kruskal-Wallis statistic = 13.53. C5) Scatter plot of the density of the RFP-tagged EB3 anterograde comets in the GC (number per $µm^2$). Kruskal-Wallis test, Dunn's multiple comparisons test, p < 0.0001, n = 25 GCs, Kruskal-Wallis statistic = 20.24. C6) Scatter plot of the density of the RFP-tagged EB3 retrograde comets in the CG (number per $µm^2$). Kruskal-Wallis test, Dunn's multiple comparisons test, p = 0.013, n = 24 CGs. Kruskal-Wallis statistic = 8.74. D1) Velocity of the RFP-tagged EB3 anterograde comets in the axon (µm s^{-1}). Violin plot. Kruskal-Wallis test, Dunn's multiple comparisons test, p < 0.0001, n = 25 axons. Kruskal-Wallis statistic = 27.00. D2) Velocity of the RFP-tagged EB3 retrograde comets in the axon (µm s^{-1}). Violin plot. One-way ANOVA, Tukey's multiple comparisons test, n=16 axons, p = 0.081, F = 2.64. D3) Velocity of the RFP-tagged EB3 anterograde comets in the GC (µm s^{-1}). Violin plot. Kruskal-Wallis test, Dunn's multiple comparisons test, p < 0.0001, n = 25 GCs. Kruskal-Wallis statistic = 33.21. D4) Velocity of the RFP-tagged EB3 retrograde comets in the GC (µm s^{-1}). Violin plot. Kruskal-Wallis test, Dunn's multiple comparisons test, p = 0.0036, n = 19 GCs, Kruskal-Wallis statistic = 11.28. E1) Fraction of time spent in pause of the RFP-tagged EB3 anterograde comets in the axon. Truncated Violin plot. One-way ANOVA, Tukey's multiple comparisons test, p = 0.0013, n = 25-29 axons. F = 7.20. E2) Fraction of time spent in pause of the RFP-tagged EB3 retrograde comets in the axon. Truncated Violin plot. Kruskal-Wallis test, Dunn's multiple comparisons test, n=21-25 axons, p = 0.086, Kruskal-Wallis statistic = 4.91. E3) Fraction of time spent in pause of the RFP-tagged EB3 anterograde comets in the GC. Truncated Violin plot. Kruskal-Wallis test, Dunn's multiple comparisons test, p < 0.0001, n = 25-31 GCs. Kruskal-Wallis statistic = 18.80. E4) Fraction of time spent in pause of the RFP-tagged EB3 retrograde comets in the GC. Truncated Violin plot. Kruskal-Wallis test, Dunn's multiple comparisons test, p = 0.26, n = 22-30 GCs, Kruskal-Wallis statistic = 2.69

Supplementary Files

This is a list of supplementary files associated with this preprint. Click to download.

- Supplementaryvideo1cometsintheaxon.avi
- Supplementaryvideo2cometsintheGC.avi
- SUPPLEMENTARYMicrotubulesarenotpassiveloadbearingelementsinaxongrowthFINAL.docx